

Evaluation of Active and Passive Gas Imagers for Transmission Pipeline Remote Leak Detection

**Final Report
December 2002**

Submitted by

Thomas A. Reichardt, Sanjay Devdas, and Thomas J. Kulp

Diagnostics and Remote Sensing Department

Sandia National Laboratories

P.O. Box 969, MS 9056

Livermore, CA 94551

and

Wayne Einfeld

Environmental Monitoring and Characterization Department

Sandia National Laboratories

P.O. Box 5800, MS 0755

Albuquerque, NM 87185

This work was sponsored by

**The Strategic Center for Natural Gas Natural Gas Infrastructure Reliability Program,
National Energy Technology Laboratory (NETL), DOE Office of Fossil Energy**



Abstract

The pipeline industry would benefit considerably from the development of systems that could provide early warning capabilities for major pipeline integrity and safety issues caused by leaks. Our effort focuses on evaluating the application of emerging active (laser-illuminated) and passive (thermal emission) approaches to detect gas leaks remotely on airborne platforms. Active and passive remote detection approaches have distinct capabilities. While passive methods allow nearly unlimited range with a simple instrumental configuration, such methods rely upon a temperature difference between the plume and the ground surface below it. Active imaging removes the thermal constraint, but requires a laser and a relatively lower operational range.

Because there are clear differences between active and passive optical detection approaches, we examined the merits of each method for the particular problem of detecting natural gas leaks in transmission pipelines. During this past year we have predicted leak concentrations and geometries, calculated detection sensitivities for active and passive approaches as a function of range, and experimentally confirmed performance predictions. In addition, for passive detection, we have examined the signal source term, measuring temperature differences between the ground and the air under different weather conditions.

Based on this study, we have chosen active detection as the optimum approach to detect natural gas leaks from a low-flying aircraft. The passive detection limit is ultimately governed by the magnitude of the energy transfer between the gas plume and the ground surface. Given a relatively modest typical temperature difference of 5°C between the ground and the air above the ground, the experimentally confirmed calculations predict that an active approach will be an order of magnitude more sensitive to detect natural gas leaks.

Table of Contents

Abstract	2
Table of Contents	3
List of Figures	4
List of Tables	5
1. Overview of Problem: Description of Detection Schemes	6
2. New Detection Technology	6
3. Design Parameters for Airborne Platform	7
4. Modeling of Leaks	9
Soil Effects	9
Atmospheric Dispersion	9
Plume Sight Paths	10
Assumptions and Caveats	11
Modeling Results	12
5. Experimental Studies and Results	13
Breadboard Active Detection System	14
System Description	14
System Evaluation	15
Breadboard Passive Detection System	18
System Description	18
System Evaluation	19
7. Consideration of different technologies	25
8. Optimal Remote Gas Imaging System for Transmission Pipeline Leak Sensing	26
Active System	27
Passive System	29
Detection Scheme Final Decision and Implementation	30
9. References	31

List of Figures

Fig. 1. Active and passive detection of gas plumes	7
Fig. 2. Airborne platform for detection of gas leaks.....	7
Fig. 3. Detection field-of-view and resolution required for airborne detection.....	8
Fig. 4. Detection scenarios: (a) raster scanning of FOV, (b) pushbroom acquisition.....	8
Fig. 5. Plume sight paths considered for calculations.	11
Fig. 6. Photograph of mobile optical laboratory.....	13
Fig. 7. Spectrum of 10 ppm-m methane in 0.038 atm-m water vapor. The asterisk designates the position of the probed absorption feature. The features in the forefront represent the absorption of methane while the features in the background represent the total absorption (methane plus water vapor).	15
Fig. 8. Design of breadboard active detection system.	15
Fig. 9. Measured signal plotted as a function of range. Also plotted is the signal intensity predicted by the model and the predicted intensity scaled (by a factor of 0.62) to fit the experimental data.....	16
Fig. 10. Illustration of plume generator.....	17
Fig. 11. Active detection of small ppm-m plumes by signal-averaging 100 data points.	18
Fig. 12. Photograph of filtered dewar.	19
Fig. 13. A/D counts of IR FPA versus temperature of imaged surface	19
Fig. 14. A/D counts versus the integration time for the target blank.	20
Fig. 15. Passive detection of 1000 ppm-m butane plumes as a function of the temperature difference between the gas and the surroundings. These images were acquired on a cloudy day.....	21
Fig. 16. Passive detection of 1000 ppm-m butane plumes as a function of the temperature difference between the gas and the surroundings. These images were acquired during nighttime.....	22
Fig. 17. Representative temperature differences between the ground surface and the air, $T_{\text{ground}} - T_{\text{air}}$	23
Fig. 18. Calculated active and passive NECLs compared to experimental results.....	25
Fig. 19. Illustration of airborne instrument deployment (modified from Fig. 2).....	27
Fig. 20. Spectra of 10 ppm-m methane in 0.038 atm-m water vapor: (a) R-branch in mid-IR, (b) Q-branch in mid-IR, (c) R-branch in far-IR, (d) Q-branch in far-IR. The features in the forefront represent the absorption of methane while the features in the background represent the total absorption (methane plus water vapor).....	28
Fig. 21. Components of proposed (a) active and (b) passive detection systems	28
Fig. 22. NECLs for active and passive detection along a single line-of-sight. A 5°C temperature difference is assumed in the calculations, and the signal attenuation due to ambient methane is included.....	29
Fig. 23. Twin Otter research aircraft.....	31

List of Tables

Table 1. Leak rates considered for calculations.....	9
Table 2. Plume sight paths considered for calculations.	10
Table 3. Path-integrated methane concentrations – very unstable.....	12
Table 4. Path-integrated methane concentrations – neutral.....	12
Table 5. Path-integrated methane concentrations – very stable.	13
Table 6. Single-shot standard deviations and NECLs for different targets and ranges	17
Table 7. Parameters of the existing breadboard systems.....	24

1. Overview of Problem: Description of Detection Schemes

The detection of gas leaks represents a critical operation performed regularly by the gas industry to maintain the integrity and safety of its vast network of piping, both above and below the ground. Below-ground piping includes approximately 400,000 miles of transmission pipelines and 1.4 million miles of distribution piping, while above-ground piping is located mainly at about 750 gas processing plants and some 3000 compressor stations. Whether addressing above or below ground gas sources, leak surveying with state-of-the-art gas detectors can be a time-consuming operation of uncertain effectiveness.

For surveys of buried piping, state-of-the-art natural gas leak detectors employ a flame ionization detector (FID). A sampling pump in the unit continuously withdraws, or “sniffs,” samples of the ambient air and delivers them through a sampling probe to the flame ionization sensor itself. The surveyor scans the ground, carrying the sampling probe barely above ground level. The probe must be brought fairly close to the leak vent to sample detectable quantities of gas. To find a leak quickly the surveyor must possess enough experience to know where to look. Complicating matters somewhat is the underground migration of leaking gas from buried pipes, causing the gas to reach the surface at some location often not apparent to the surveyor. Leak surveys with an FID can cover 8-10 miles per day in the man-portable mode, and slightly more in a vehicle-mounted mode. As an alternative to using an FID, low-flying aircraft are sometimes used to discern discolored vegetation caused by the gas leaks. This technique obviously cannot be used effectively in areas without sufficient vegetation, such as the desert and steppe areas or during the winter.

2. New Detection Technology

Based on these considerations, it would be desirable to develop a remote pipeline inspection instrument that could detect the leak remotely without physically sampling the air above the leak. Such a system might be implemented on an aircraft or even a satellite. There are two alternatives for such remote sensing techniques: (1) active detection, which requires illuminating the scene with a radiation source, usually a laser, that is absorbed by the target gas, and (2) passive detection (also called thermal detection), which relies on radiative transfer due to a temperature and/or emissivity difference that usually exists between the background and the target cloud (see Fig. 1). While passive methods allow nearly unlimited range with a simple instrumental configuration, these methods rely upon a thermal flux between the plume and the ground surface below it. Active detection removes the thermal constraint, but requires a laser and a scattering surface behind the gas for generation of the signal. It also has a relatively lower operational range. In comparison to sampling probes, these remote detection technologies possess several advantages:

- They provide the potential for faster monitoring, and more frequent inspection for leaks (as caused by external infringements, material fatigue, etc.).
- By visualizing the entire leak rather than sampling a particular volume of air, they allow for more accurate pinpointing of the leak location, decreasing pipe excavation costs once the leak is detected.
- They allow a more complete and effective coverage of pipeline right-of-ways where leaks might migrate.
- They depend less on operator experience and judgment for leak detection.
- They provide the ability to monitor inaccessible, or “over the fence,” areas.

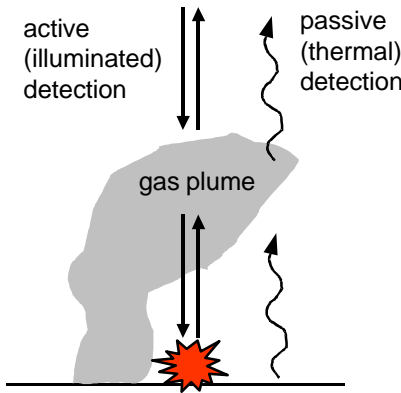


Fig. 1. Active and passive detection of gas plumes

3. Design Parameters for Airborne Platform

For analysis of airborne remote leak detection, we will begin with the operational parameters of the low-flying aircraft used to discern discolored vegetation. This is illustrated in Fig. 2. It was reported by industrial representatives that aircraft fly at an altitude of ~200 m at a speed of ~120 mph for detection of discolored vegetation. For remote optical detection of methane, we assume that we will probe a 10-m side-to-side area at a resolution of 0.5-m (Fig. 3).

Remote detection of transmission pipeline leaks will likely require sweeping the detector field-of-view (FOV) over the area of interest to acquire an image of the integrated methane concentration between the aircraft and the ground surface. For active detection, this can be accomplished by either dithering a laser beam back and forth across the field of view (often referred to as raster scanning, see Fig. 4a) or by spreading the laser beam so that it encompasses the necessary field of view (referred to as pushbroom acquisition, see Fig. 4b). For passive detection, the image will require frequent acquisition of the field of view by, for example, a linear array detector. Because of the speed of airborne travel, the acquisition must be performed at a rapid rate to cover the required ground space within the area of interest. For a raster-scanning measurement at 120 mph, the FOV must be swept between measurement pixels at a rate of 2140 Hz. For pushbroom acquisition, this data rate is lowered by a factor of 20 to 107 Hz.

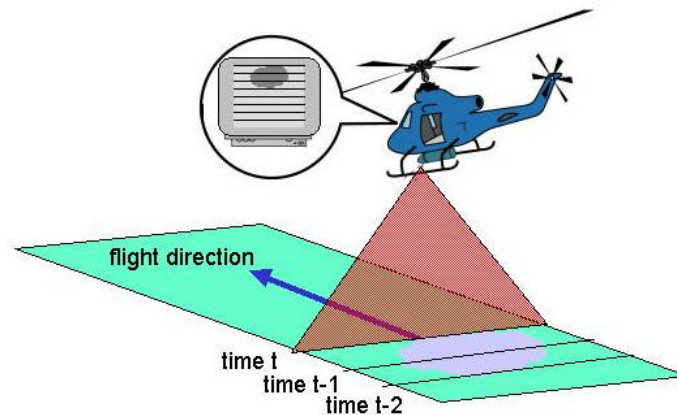


Fig. 2. Airborne platform for detection of gas leaks

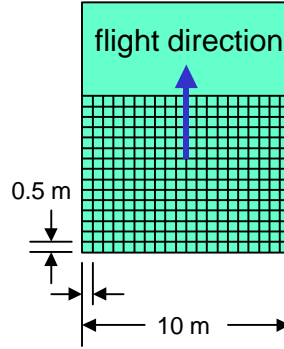


Fig. 3. Detection field-of-view and resolution required for airborne detection.

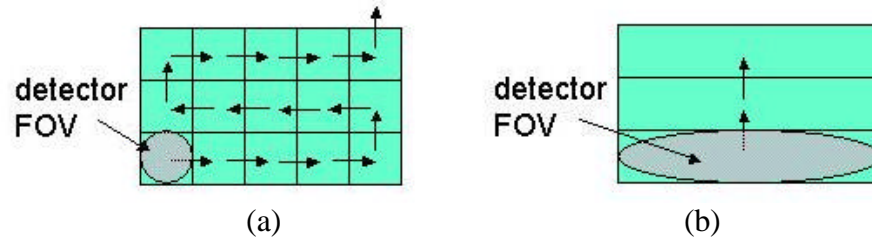


Fig. 4. Detection scenarios: (a) raster scanning of FOV, (b) pushbroom acquisition.

Before prescribing an optically-based leak detection device for the transmission sector, we recognized the four boxed questions below required further study.

- (1) *What is the integrated column density of natural gas that will need to be detected for transmission pipeline leaks?*
- (2) *What are the instrument limitations that could affect the detection of methane leaks?*
- (3) *How do active and passive techniques theoretically compare for airborne stand-off distances?*
- (4) *What are the most important performance factors that can be improved for detection of transmission pipeline leaks?*

To address the first question, we undertook a modeling analysis of the distribution of the natural gas plume under a variety of conditions. Using this analysis, we calculated the integrated column density of natural gas that will be detected from an airborne platform (Section 4). We addressed the second question by constructing active and passive detection systems and comparing their performance to theoretical predictions (Section 5). This served as a benchmark for assessing the predictive accuracy of our active and passive detection analysis. The third question was addressed by performing a detailed analysis of the signal generation for active and passive detection of natural gas plumes (Section 6). This analysis allowed us to calculate the detection limits for systems that we can construct in the laboratory for testing. After considering potential modifications on the measurement approaches (Section 7), we used the experimentally

tested analysis to address the fourth question, predicting the performance improvements afforded by modifying the existing detection schemes. We then prescribe an airborne remote sensing device in Section 8.

4. Modeling of Leaks

A preliminary modeling effort presented in the project proposal looked at an axisymmetric plume derived from an exposed jet (no soil overburden) under quiescent conditions. The modeling effort presented here takes both soil effects and meteorology into account. An attempt to understand soil conditions and how they might influence subsurface methane leak dynamics was undertaken via a literature search; however, the search yielded no useful information. The lack of specific information pertaining to methane leak pathways through soil was corroborated in discussions with industry personnel in Albuquerque in 11/01.

Soil Effects

In the absence of better information, a crude approximation was carried out using the following reasoning: in the extremes, one is likely to encounter either compact, dense soil (such as clay) or loose, non-compact soil (such as sand) as overburden for a buried gas pipe. It can be further assumed that a subsurface leak path through compact soil will be less diffuse than what would be observed through sandy soil. In either case, a single leak path to the surface is unlikely. Instead, multiple leak paths will develop and the degree of soil compaction is assumed to be inversely proportional to the number of leak paths to the surface. That is, dense soil produces fewer leak paths and loose soil produces many leak paths. Multiple leak paths through the soil to the surface result in an effective methane area source at the surface. In an attempt to bound the leak problem, surface leak areas are assigned, albeit somewhat arbitrarily. Using this approach, the problem is bounded on either end (compact and loose soil) for the purposes of evaluating the ability of various remote sensing technologies to detect the resulting plume. For a compact soil a source leak area of 1 m^2 is assumed. At the other extreme, for a non-compact soil type a source area of 100 m^2 is assumed. Two methane leak rates, shown in Table 1, are taken from calculations involving realistic hole sizes and internal pipe pressures such as might be encountered in a transmission pipeline.

Table 1. Leak rates considered for calculations.

Leak Scenario	Leak Rate (scf/hr)	Leak Rate (g/s)
0.0031-in ² hole, 400 psi internal pressure	324	1.67
0.0123-in ² hole, 1000 psi internal pressure	2088	10.7

Atmospheric Dispersion

For estimation of the atmospheric dispersion of the plume, a simple Gaussian dispersion model is used. Input parameters for this modeling approach include the following: leak rate, source area, release height, wind speed, and atmospheric stability class. The atmospheric stability class is related to the temperature structure of the atmosphere, which in turn is influenced by the amount of solar heating at the ground level. On a hot sunny day, ground heating results in the convective heating of the air near the ground. Warm air near the ground

propagates upward producing air turbulence which in turn causes more rapid dispersion of the plume in both the horizontal and vertical directions. On the other hand, under highly stable conditions (for example, a clear cold night) the opposite conditions can occur. The ground cools by radiative loss. The air near the ground is convectively cooled and is non-buoyant—this is commonly referred to as a temperature inversion. The stagnant cool air near the surface is non-turbulent and thus plume dispersion in the horizontal and vertical directions is considerably reduced. The intermediate condition is often termed neutral stability. In this case the vertical temperature structure of the atmosphere is such that significant vertical air motion does not occur in either direction and the resulting atmospheric turbulence and methane dispersion is in the intermediate range.

Plume Sight Paths

As in the axisymmetric analysis, three sight paths are used to estimate the path-integrated methane concentrations that would result under the various leak rates, source areas, wind speed, and atmospheric stability conditions. The sight paths are given in Table 2 and are illustrated in Fig. 5. We considered a square ground level area source with the following coordinate system: the point x, y , and $z = 0$ m is at the center of the square. The x direction is downwind horizontal, the y direction is crosswind horizontal, and the z direction is vertical.

Table 2. Plume sight paths considered for calculations.

Sight Path	View angle	Location
Path 1	Nadir view	5 m downwind from the center of the area along the plume axis ($x = 5$ m, $y = 0$ m, $z = 0$ to 20 m)
Path 2	Nadir view	20 m downwind from the center of the area and offset 20 m from the plume axis ($x = 20$ m, $y = 20$ m, $z = 0$ to 20 m)
Path 3	Horizontal view	25 m downwind from the center of the area looking perpendicular to the wind direction at an elevation 1 m above ground. ($x = 25$ m, $y = -35$ to 35 m, $z = 1$ m)

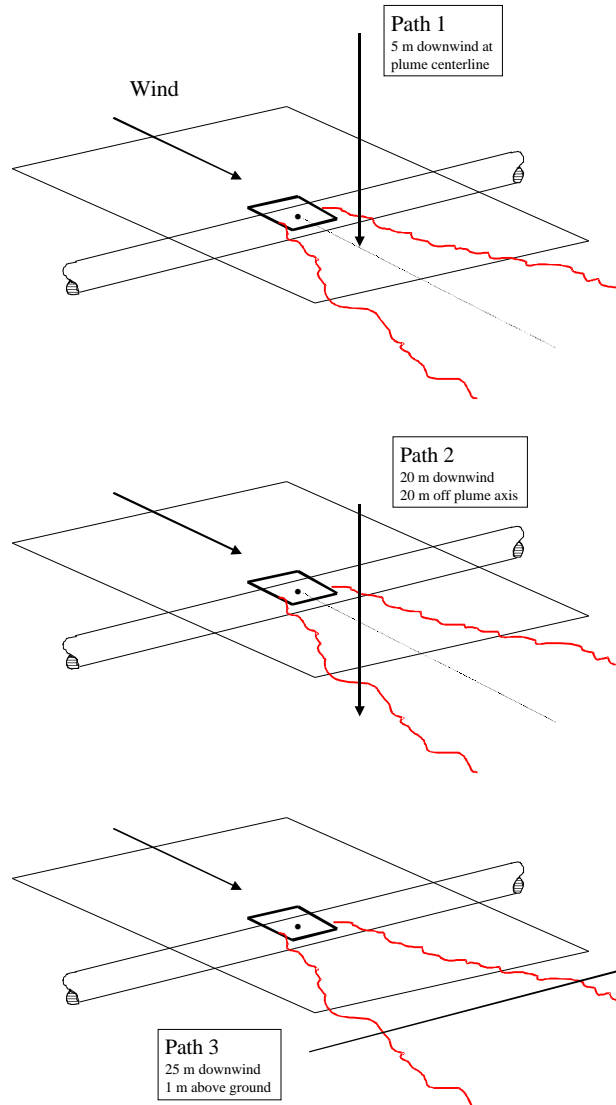


Fig. 5. Plume sight paths considered for calculations.

Assumptions and Caveats

- No methane buoyancy effects exist at the area source because the leak rates are low, the methane is quickly diluted to very low levels, and the density is effectively that of air.
- The release height is assumed to be at ground level ($z = 0$ m).
- The area source is really a line source that slices through the mid-point of the area perpendicular to the wind direction. The line source strength is normally distributed with the peak at the center point of the area.
- The plume dispersion parameters used for the plume dispersion calculations are based on experimental measurements and are derived from 3-minute averages. Wind meander (the normal variation of wind direction with time) will result in a more spatially dispersed plume and correspondingly lower plume concentrations over longer averaging intervals. For relatively high-speed remote sensing applications this factor should not be important.

- The interaction of the wind speed at the ground is difficult to model as it depends strongly on the surface roughness. These surface roughness effects are ignored.
- No local topography is considered in these calculations.

Modeling Results

Modeling results are shown for three stability classes (very unstable, neutral, and very stable) in the following three tables. The value given is the path-integrated methane concentration in units of ppm-m. Methane background levels are not taken into account in the values shown.

Table 3. Path-integrated methane concentrations – very unstable.

Leak Rate scf/hr	Leak Area m²	Wind Speed m/s	Path 1 ppm-m	Path 2 ppm-m	Path 3 ppm-m
324	1	1	845	1.17	495
324	1	10	84.5	0.12	49.5
324	100	1	312	7.20	402
324	100	10	31.2	0.72	40.2
2088	1	1	5410	7.51	3170
2088	1	10	541	0.75	317
2088	100	1	2000	46.1	2570
2088	100	10	200	4.61	257

Table 4. Path-integrated methane concentrations – neutral.

Leak Rate Scf/hr	Leak Area m²	Wind Speed m/s	Path 1 ppm-m	Path 2 ppm-m	Path 3 ppm-m
324	1	1	2810	<0.001	912
324	1	10	281	<0.001	91.2
324	100	1	473	<0.001	672
324	100	10	47.3	<0.001	67.2
2088	1	1	18000	<0.001	5850
2088	1	10	1800	<0.001	585
2088	100	1	3030	<0.001	4310
2088	100	10	303	<0.001	431

Table 5. Path-integrated methane concentrations – very stable.

Leak Rate Scf/hr	Leak Area m ²	Wind Speed m/s	Path 1 ppm-m	Path 2 ppm-m	Path 3 ppm-m
324	1	1	5840	<0.001	827
324	1	10	584	<0.001	82.7
324	100	1	507	<0.001	809
324	100	10	50.7	<0.001	80.9
2088	1	1	37400	<0.001	5300
2088	1	10	3740	<0.001	530
2088	100	1	3250	<0.001	5180
2088	100	10	325	<0.001	518

5. Experimental Studies and Results

Below we describe the experimental evaluation of active and passive detection schemes. Due to the scoping nature of this study, the breadboard systems are designed for implementation into the mobile optical laboratory shown in Fig. 6. Off-the-shelf commercial optical components are used, and detailed component integration is unnecessary. After summarizing the breadboard systems, we describe tests that have been performed to examine the relative effectiveness of gas plume detection. For both the active and passive systems, these tests can be summarized by the following four steps:

- (1) *Evaluate absolute magnitude of optical signal (photons) and compare with predictions*
- (2) *Measure baseline noise and compare with predictions*
- (3) *Demonstrate detection of controlled gas plumes*
- (4) *Evaluate effects of system-dependent limitations*



Fig. 6. Photograph of mobile optical laboratory.

Breadboard Active Detection System

System Description

Methane plumes are detected by active methods when they absorb backscattered infrared (IR) radiation in a laser-illuminated scene. The source term for active detection is a function of the concentration-length (CL) product of the target plume as well as the reflectivity of the background scattering surface. To maximize the laser attenuation, the spectral profile of the laser must be narrower than the methane absorption linewidth and must be centered at the peak of the strongest absorption line that is not affected by interfering species. The strongest absorption band in the mid-IR is the ν_3 rovibronic band centered at $\sim 3018\text{ cm}^{-1}$. The optimal absorption feature in that band was found to be at 3057.7 cm^{-1} . Fig. 7 contains a plot of a portion of the ν_3 band including this feature, calculated for a single pass through a methane plume density of 10 ppm-m. The calculation also assumed the presence of the only significant interferent (water vapor) present at a density of 0.038 atm-m. It is evident that this concentration of methane will produce a roundtrip optical depth of 0.11 and will not overlap significantly with water vapor.

The breadboard system for active detection is illustrated in Fig. 8. A pulsed optical parametric generator (OPG) produces the $\sim 3.3\text{-}\mu\text{m}$ radiation absorbed by the methane plume. The repetition rate is 120 Hz and the typical pulse energy is 10 μJ . This illumination source is similar to that described by Reichardt et al.¹ However, unlike that work, this breadboard system has been implemented in the mobile optical laboratory to test the sensitivities in field environments with similar ranges and backgrounds to those probed for transmission pipeline leaks. The output of the pulsed OPG is directed to the probed target area, and the receiver optics collect radiation that is backscattered from a surface behind the gas plume.

The pulsed OPG is used to detect a differential signal that is a function of the column-integrated methane concentration. For differential detection, the scene is illuminated at two wavelengths: one corresponding to the peak of the methane absorption feature (termed the “on-wavelength”) and one tuned away from the absorption feature (termed the “off-wavelength”). The column integrated methane concentration is calculated by taking the natural logarithm of the ratio of the on-wavelength signal to the off-wavelength signal. This effectively eliminates image features in the background, increasing the visibility of the methane column density. In practice, the wavelength of the pulsed output is dithered on and off the methane absorption feature for every other laser firing. The \ln -ratio of the two successive shots on and off the absorption feature is then calculated to determine the path-averaged methane concentration.

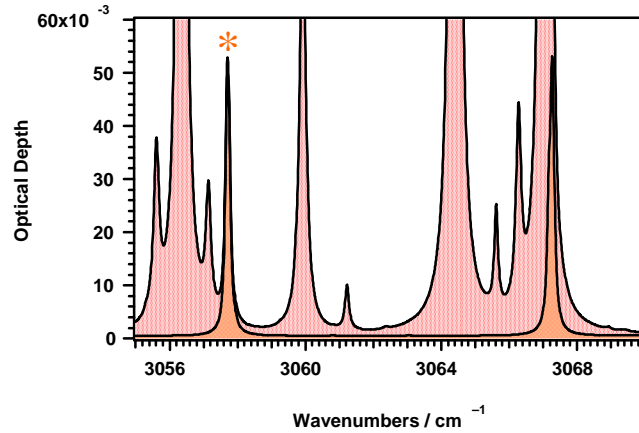


Fig. 7. Spectrum of 10 ppm-m methane in 0.038 atm-m water vapor. The asterisk designates the position of the probed absorption feature. The features in the forefront represent the absorption of methane while the features in the background represent the total absorption (methane plus water vapor).

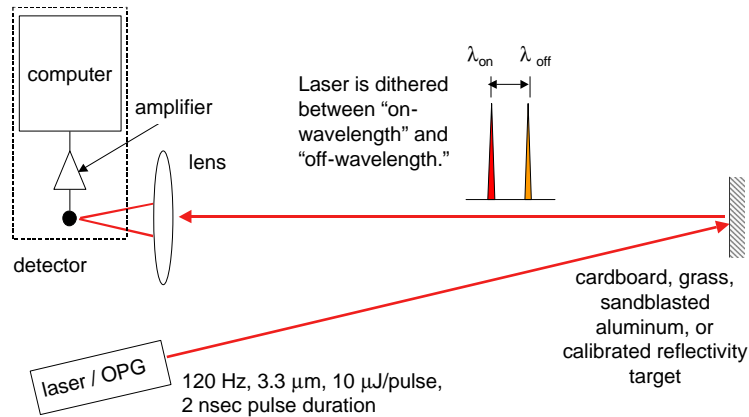


Fig. 8. Design of breadboard active detection system.

System Evaluation

- (1) *Evaluate absolute magnitude of optical signal (photons) and compare with predictions:* We have compared the signal strength calculated with the standard lidar equation to that acquired with the breadboard system. The results are within a factor of two from the theoretical return signals (see Fig. 9).

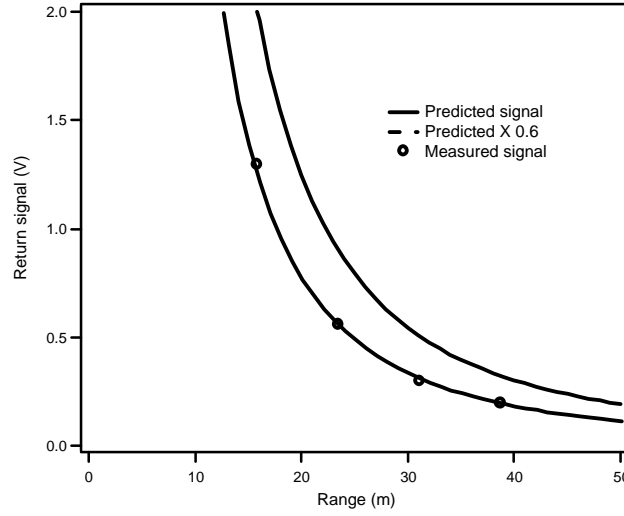


Fig. 9. Measured signal plotted as a function of range. Also plotted is the signal intensity predicted by the model and the predicted intensity scaled (by a factor of 0.62) to fit the experimental data.

- (2) *Measure baseline noise and compare with predictions:* We have measured the baseline noise off of both stationary and moving targets. This noise level has been converted into an equivalent CL product and compared to the NECL calculated for active detection. The results are summarized in Table 6. Because the return signal is inversely dependent on the square of the standoff distance, at short distances laser speckle noise limits the NECL. When a laser beam is scattered from a hard target, an interference pattern is created which is termed speckle. The speckle standard deviation can be calculated with the formula

$$\text{fractional noise} = \frac{4\lambda}{\pi d_{\text{receiver}} \theta_l},$$

where λ is the laser wavelength (m), d_{receiver} is the diameter of the receiver lens (m), and θ_l is the full-angle divergence of the laser beam (radians). If the laser divergence is optimally matched to the receiver divergence,

$$f_{\#} = \frac{d_{\text{detector}}}{d_{\text{receiver}} \theta_l},$$

then the speckle noise becomes a function of the $f_{\#}$ of the receiver optic as

$$\text{fractional noise} = \frac{4\lambda f_{\#}}{\pi d_{\text{detector}}},$$

where d_{detector} is the detector diameter (m). With the parameters of the active system (listed in detail in Table 7) we calculate a speckle noise of 1.7%. This is in agreement with the noise observed from scattering off of moving targets at short (16 m) distances. For stationary objects, the noise is reduced because the detector is repeatedly sampling the same speckle pattern over time.

Table 6. Single-shot standard deviations and NECLs for different targets and ranges

Target and Range (stationary unless otherwise indicated)	Single-shot std. dev. (%)	Single-shot NECL (ppm-m)
Cardboard at 16 m	1.2	1.2
Cardboard at 16 m (moving)	1.8	1.8
Grass at 16 m	1.5	1.5
Grass at 16 m (moving)	1.8	1.8
Grass at 30 m	3.5	3.5
Sandblasted aluminum at 100 m	4.7	4.7
Grass at 100 m	8.0	8.0

- (3) *Demonstrate detection of controlled gas plumes:* We tested the active detection system by measuring methane emitted at controlled flow rates from a plume generator illustrated in Fig. 10. This generator allows us to vary the flow speeds of the methane and air. For calculation of the CL product, we could approximate the flow as relatively uniform over the tube area. The minimum detectable limit is, in practice, 3 to 5 times the NECL. To differentiate the laser absorption by the gas from the system noise, we periodically inserted and then removed the plume while acquiring data. Fig. 11 displays an example of the small CL-product plumes that we have detected by signal averaging 100 data points. The initial 200 time-units in Fig. 11 display the baseline noise, after which plumes of increasing concentration were subsequently released and detected.

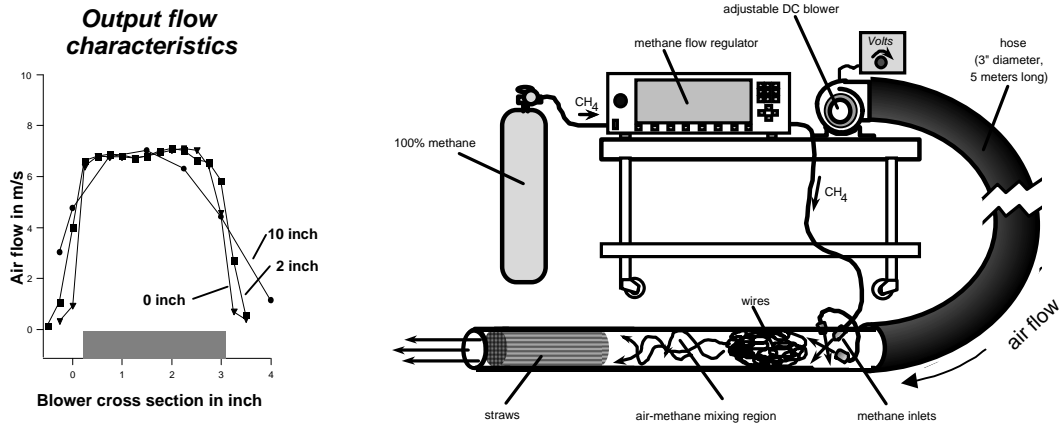


Fig. 10. Illustration of plume generator

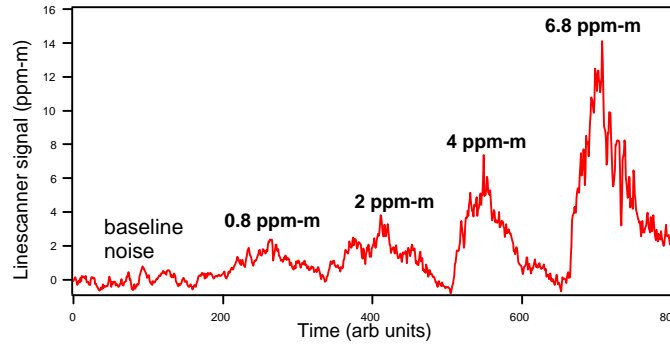


Fig. 11. Active detection of small ppm-m plumes by signal-averaging 100 data points.

- (4) *Evaluate effects of system-dependent limitations:* The above tests were performed for standoff distances of 15 to 30 m, easily accessible with the breadboard system. These tests are sufficient for testing noise sources that are independent of target range, such as speckle and electronic noise. However, there will be sources of interference (e.g., atmospheric scintillation and water vapor absorption) that will increase with target range, and it is important to evaluate these sources by performing tests at longer standoff distances. To acquire sufficient signal strength at longer distances with the breadboard system, we used a sandblasted aluminum target that provides a diffuse scattering surface with a large reflectivity of 0.28 sr^{-1} .² The standard deviation of the return signal could then be compared to the return signal off of a grass background (estimated reflectivity of 0.001 sr^{-1}), which suffered from low signal strength. The return signal noise from this sandblasted target at 100 m should be similar to that of cardboard and grass at 16 m. However, the range-dependent noise sources contribute significantly to the standard deviation of the return signal. As displayed in Table 6, the single-shot standard deviation for the sandblasted aluminum target is 4.7% at 100 m, significantly above the speckle noise limit.

Breadboard Passive Detection System

System Description

Methane plumes are detected by passive methods when radiative transfer occurs between the plume and the surroundings. The source term for passive detection is a function of the CL product of the target plume as well as the emissivity of the background and the temperatures of the target plume and the background. Because the detector measures the radiant exchange, evaluation of the system performance is equivalent to characterizing the radiance sensitivity of the instrument.

To perform this characterization, we have modified an infrared camera in our laboratory (Fig. 11) for passive methane detection. The camera (Model AE-173, Amber Engineering, Goleta, CA) is based on a modified cooled InSb 256×256 array that has a snapshot-mode, direct-injection (DI) readout. The array is housed in a pour-cooled dewar that is typically operated at 77 K. It is fitted with an $f/2.3$ 100-mm effective focal-length lens.

For detection of methane, the light from the scene is spectrally filtered for wavelengths that are absorbed by methane and for wavelengths that are not absorbed by methane. Because methane has narrow absorption features, it is ideally detected with a spectrally narrow filtering system (i.e., a grating spectrometer), but the construction of such a system is beyond the scope of this project. The filtered dewar was instead tested for the detection of butane. Unlike methane,

with its narrow absorption features, butane has a spectrally broad absorption feature at $\sim 3.4 \mu\text{m}$. A broad filter is ideally suited for sensing butane plumes, and the results of this study can be used to examine the design of a narrow-band passive detection system for methane. In practice, butane was detected by toggling between the wavelengths absorbed by butane and those not absorbed by butane. The filter wheel allows us to toggle between the two wavelengths at a rate of $\sim 1 \text{ Hz}$. In Section 6, we will use the results of analyzing the spectrally broader detection scheme to evaluate more advanced filtering systems.

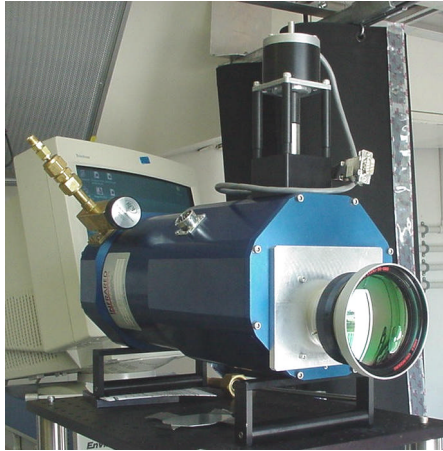


Fig. 12. Photograph of filtered dewar.

System Evaluation

- (1) *Evaluate absolute magnitude of optical signal (photons) and compare with predictions:* To test the number of photons arriving at the detector for the passive system, we have observed the effect of varying the temperature of an imaged surface on the signal registered at the detector. As shown in Fig. 13, excellent agreement is obtained between the predictions and experimental data. A single A/D count represents 298 electrons.

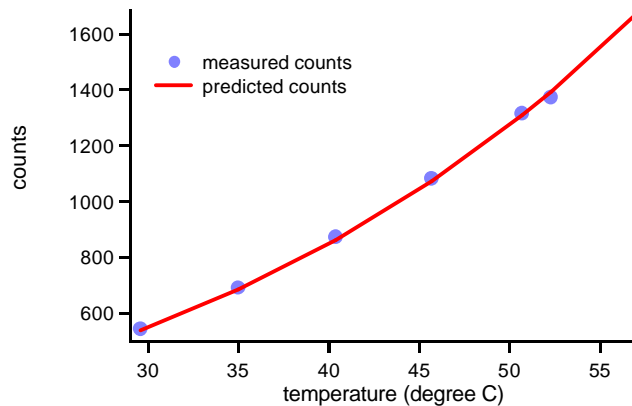


Fig. 13. A/D counts of IR FPA versus temperature of imaged surface

- (2) *Measure baseline noise and compare with predictions:* To calculate the FPA noise, we note that it has various sources. These sources include shot noise, dark current noise, offset noise,

read noise, digitization noise, and array nonuniformity noise. We measured the contributions of these noise sources with the experiments described below.

- (a) The absolute magnitude of the offset and dark current were determined by exposing the FPA to the target blank (a disk at 77 K) for different exposure times. Typical results are shown in Fig. 14. The offset is measured as the y-intercept of 620 counts, while the slope corresponds to a dark current of 14 pA. The specified read noise is a few hundred electrons ($300 e^-$).

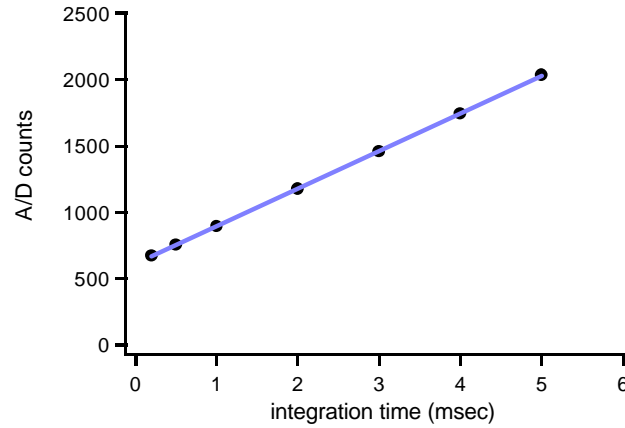


Fig. 14. A/D counts versus the integration time for the target blank.

- (b) The combined effects of dark current, offset, read noise, and digitization noise were evaluated by measuring the standard deviation on a single array pixel for a series of frames at low photon flux by exposing the FPA to the target blank. We measured the standard deviation to be 0.7% with a mean count of 870 ($2.6e+05$ electrons). The exposure time was 5 msec.
- (c) The combined effects of all sources of noise in (b) with the addition of shot noise were evaluated by measuring the standard deviation on a single array pixel for a series of frames at high photon flux. We have measured this to be 0.7% with a mean count of 3592 ($1.1e+06$ electrons).
- (d) Finally, the effect of nonuniformity noise was evaluated by flooding the array with uniform light with the nonuniformity correction activated. The standard deviation of all pixels from the mean was then measured to be 1.5% with a mean count of 3359 ($1.0e+06$ electrons).
- (3) *Demonstrate detection of controlled gas plumes:* We have used the passive detection system to analyze the ability to detect butane plumes with thermal radiation. We have used the filtered FPA to examine the measurable CL product of butane using the plume generator illustrated in Fig. 10. The detection limit is a function of temperature, as displayed in Fig. 15 and Fig. 16.

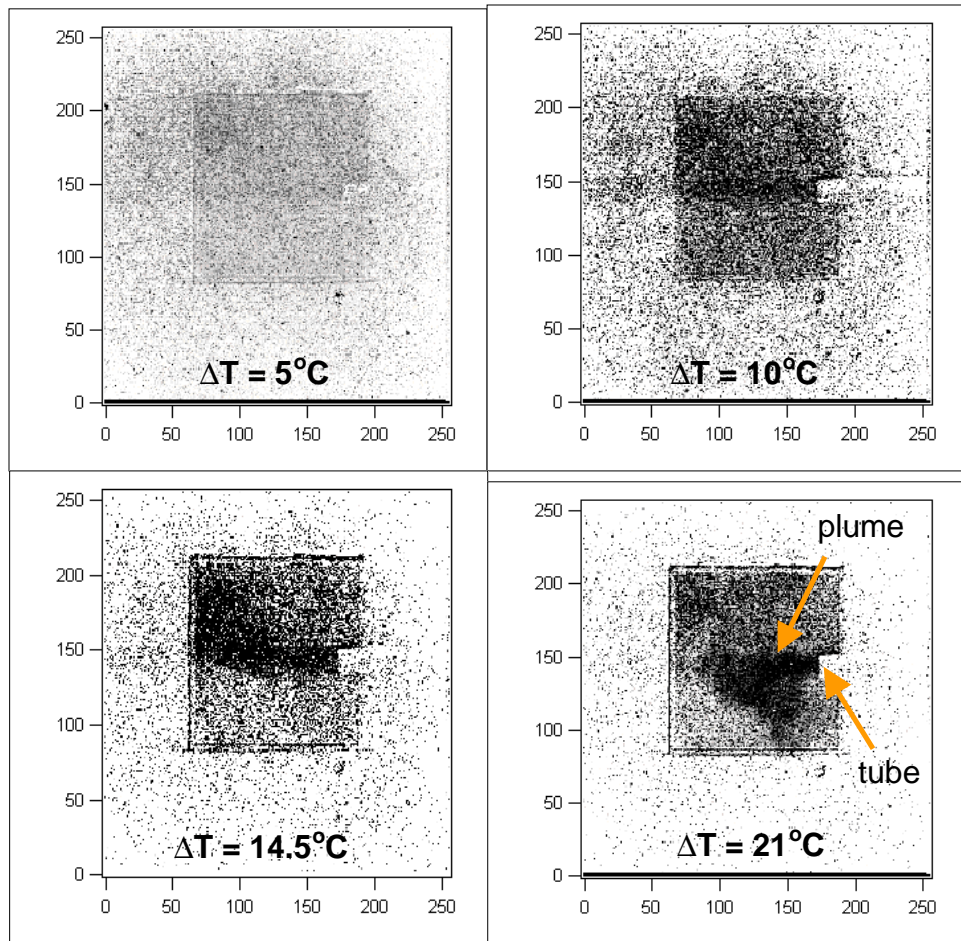


Fig. 15. Passive detection of 1000 ppm-m butane plumes as a function of the temperature difference between the gas and the surroundings. These images were acquired on a cloudy day.

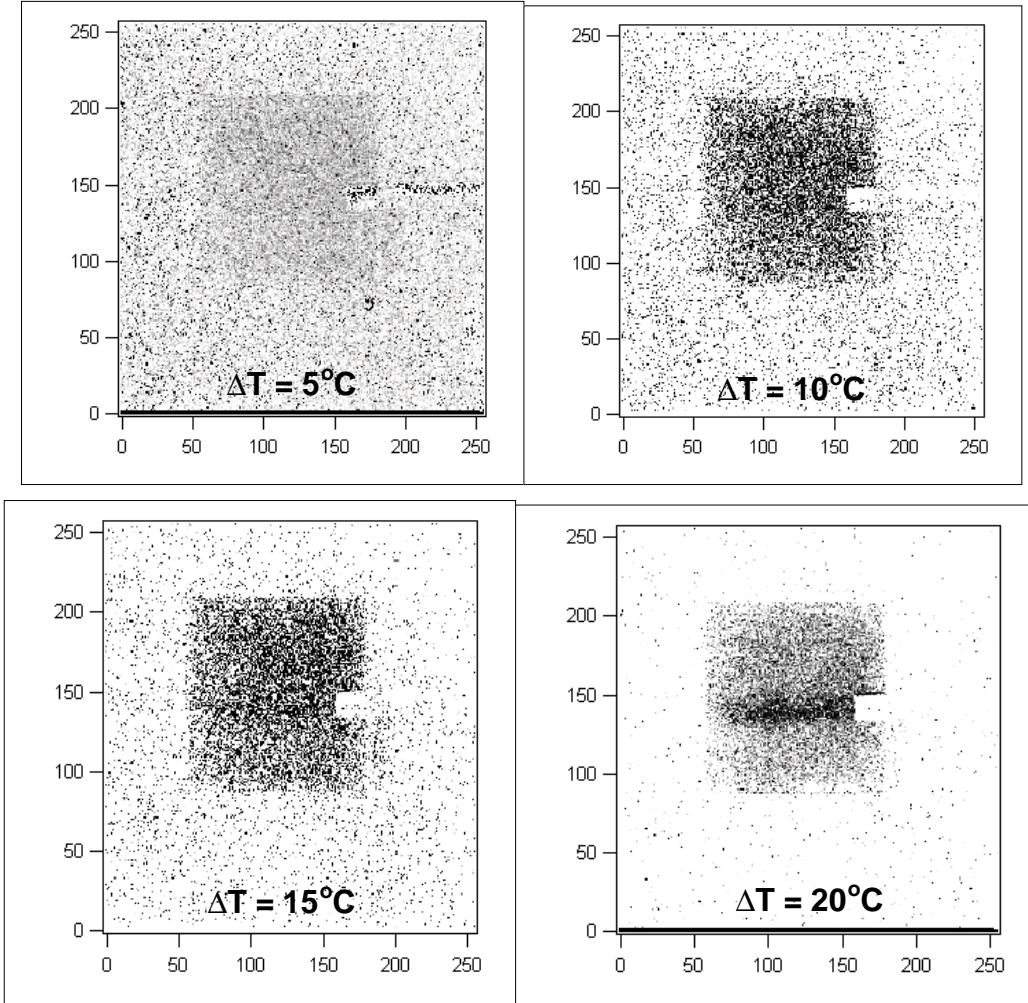


Fig. 16. Passive detection of 1000 ppm-m butane plumes as a function of the temperature difference between the gas and the surroundings. These images were acquired during nighttime.

- (4) *Evaluate effects of system-dependent limitations:* We have ratioed two successive scenes at closely spaced wavelengths to evaluate the effect of measuring thermal radiation at two wavelengths. This noise source is analogous to reflectivity variations for the active detection system. This measurement defined the noise floor for our passive detection scenario, and served to assess the NECL for typical operations in developing a passive detection device. The standard deviation was 2.8% over the pixel values. This image noise is compared to predicted noise levels in Section 6.

6. Modeling of Detection Systems

The source term for active detection depends on the laser energy and the reflectivity of the backscattering surface. These values can be reliably estimated based on laser parameters and tabulated reflectivity values for typical backscattering surfaces (e.g., sand, soil, and grass). On the other hand, the source term for passive detection depends on the temperature difference between the ground surface and the gas plume. To evaluate the detection of the gaseous plume

in contrast with the surroundings, the plume is approximated to assume the temperature of the surrounding air once it is emitted into the atmosphere. The temperature difference between the ground and the air above it will be a strong function of the weather conditions, and we therefore undertook a study of the typical temperature differences we expect to see from an airborne platform. Fig. 17 displays representative temperature measurements acquired at the ground surface and the air for different heights above the ground. While within an inch from the ground the air temperature is similar to the ground temperature, further from the ground we see that the temperature difference between the ground and the air above it exceeds 10°C during the afternoon hours for all days considered. As a representative estimate of the temperature difference, we chose 5°C .

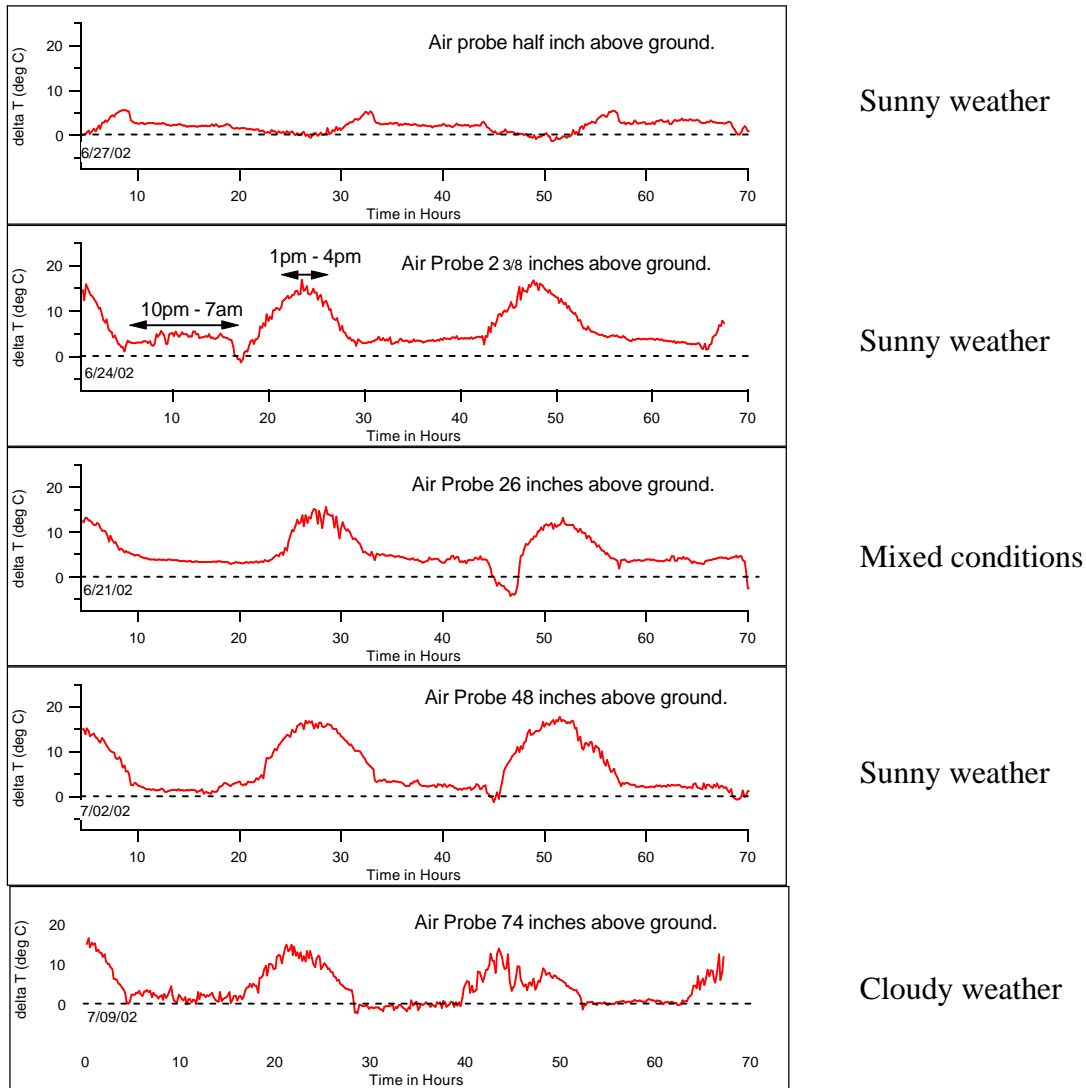


Fig. 17. Representative temperature differences between the ground surface and the air, $T_{\text{ground}} - T_{\text{air}}$.

We have developed a mathematical model to analyze the relationship between the detection limit and the target distance. The work of Flanigan³ was used as a basis for this model, but we have added the effects of background emissivity, absorption linewidth, spectral resolution, and

differential detection. A detailed derivation of the modeling is included in the report by Reichardt et al.⁴ Table 7 summarizes the input parameters required to model the performance of the breadboard systems.

Table 7. Parameters of the existing breadboard systems.

Parameter	Passive (Thermal)	Active (Illuminated)
Absorptivity	1e-04 ppm ⁻¹ m ⁻¹ (butane)	5e-03 ppm ⁻¹ m ⁻¹ (methane)
Center frequency	2869 cm ⁻¹	3057.7 cm ⁻¹
Filter bandwidth	63 cm ⁻¹	63 cm ⁻¹
f/#	2.3	1
Focal length	100 mm	88 mm
Lens diameter	43 mm	88 mm
FOV	0.34 mrad (for array pixel)	2.8 mrad (for single-element detector)
Throughput	1.3e-06 cm ² sr	7.5e-04 cm ² sr
Collector area	15 cm ²	61 cm ²
ΔT (and ϵ_B) or energy (and reflectivity)	5°C ($\epsilon_B = 1.0$)	10 μ J (reflectivity = 0.001 sr ⁻¹)
Scan/pulse	3.2 msec	2 nsec
Bandwidth	313 Hz	0.5 GHz
Quantum efficiency	1.0	1.0
Sensor transmittance	0.825	0.72

Fig. 18 displays the comparison between the predicted active and passive system performance, as well as the accompanying experimental data from Table 6. For short distances, we speculate that the larger measured NECL for the active system is due to movement of the grass. However, for longer distances, the measured NECL is actually smaller than that predicted by the model, owing to the larger reflectivity for grass as compared to the assumed reflectivity of 0.001 sr⁻¹. Nevertheless, the model predicts the behavior of the NECL to within a factor of 3 for the distances examined.

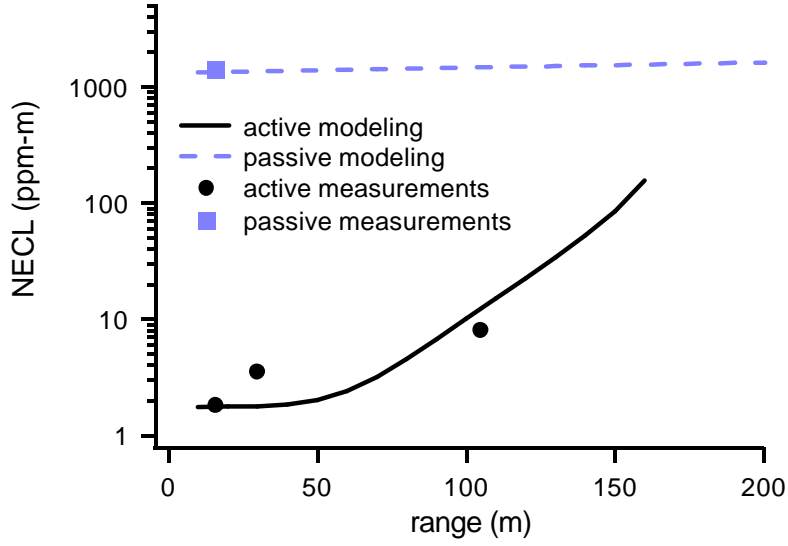


Fig. 18. Calculated active and passive NECLs compared to experimental results.

7. Consideration of different technologies

In conducting a study of potential instruments, we have considered possible improvements over the active and passive techniques described here. We will term the techniques described thus far as the baseline detection scenarios. The baseline passive technique is therefore to use a filter or dispersive grating to detect passive radiation from two closely spaced wavelengths, one of which includes the absorption feature of the gas to be detected. The baseline active technique is topographic differential backscatter using a pulsed laser source.

The *Michelson Interferometer-Spectrometer*, or *FTIR*, have been shown to possess the ability to capture a single spectrum at sufficient spectral resolution for methane detection in ~1 sec, which would not be suitable for airborne detection for which we need to acquire data at ~100 Hz.

Laser heterodyne techniques can be used to reach the shot-noise limit, but have limited throughput. These techniques operate by mixing a local oscillator (e.g., a modulated laser source) with the active or passive radiation that is captured by the detector. For optimized performance, the receiver should collect only a single speckle cell. This decreases the throughput by a large factor. If we define the throughput by $Th = A_C \Omega_C$, where $\Omega_C = \pi \theta_{1/2}^2$, and the size of a speckle cell is $\lambda^2 / \pi \theta_{1/2}^2$, then the optimal throughput for a laser heterodyne receiver is given as λ^2 . In comparison with the baseline systems, the throughput is decreased by three orders of magnitude at 3 μm . Calculations have shown that this would have an overall negative effect on the system detection limit. Heterodyne detection in the long-wave IR could be beneficial, however, because of the increased throughput and the increased radiative flux at this wavelength range.

Gas correlation spectroscopy can be used for either passive or active sensing to separate the wavelengths absorbed and unabsorbed by the probed gas. It works by having two detector legs, one of which has a gas cell with the absorbing species in the path. When the signal returns, it is

split between the two legs, and the difference between the signals is recorded. For active techniques, this approach is useful when the source is broadband and you are attempting to isolate the components of the radiation that are absorbed and not absorbed. This eliminates noise from laser energy fluctuations and reduces the need to have successive pulses temporally closely spaced. However, spreading the spectral shape of the pulse over a wavelength range both absorbed and unabsorbed by the target gas significantly decreases the SNR acquired at both wavelengths. Minato et al.⁵ report a methane NECL of 88 ppm-m for averaging the return signal from eight laser pulses. Similarly, in a passive approach, the technique sacrifices the potential detection limit for the advantage of simplicity. Sandsten et al.⁶ report a detection limit of 200 ppm-m of ammonia (a strong infrared absorber) with a temperature difference of 18 K and a 15 Hz acquisition rate. Gasoptics (Lund, Sweden) is currently marketing a device based on passive gas correlation spectroscopy as a method for detecting gas leaks.

Depending on the primary source of noise, *frequency modulation (FM)* can increase the SNR of absorption signals by many orders of magnitude. A full comparison of FM spectroscopy with the baseline case is difficult, because FM detection of methane is generally performed with diode lasers operating in the near-IR telecommunications wavelengths⁷ ($\sim 1.6 \mu\text{m}$). The absorptivity of methane at these wavelengths is a factor of 100 less than the absorptivity in the mid-IR. For a full discussion of the application of FM methods with remote sensing, the reader is referred to the paper by Dubinsky et al.⁸ A recent study by Wainer et al.⁹ displayed an NECL of 12 ppm-m for a 30-m standoff distance and a 1-sec acquisition time. This NECL is two orders of magnitude worse than demonstrated by our current system in Fig. 11.

8. Optimal Remote Gas Imaging System for Transmission Pipeline Leak Sensing

In prescribing a remote gas sensing system, we have assumed the operational parameters of the low-flying aircraft used to discern discolored vegetation. We considered two instruments, one active and one passive, which would be suitable for airborne deployment. To meet the goal of airborne detection of methane under the assumed budget of two performance periods we designed the system to measure gas concentrations along a single line of sight approximately 0.5-m wide as the aircraft flies over the pipeline, as illustrated in Fig. 19. While limiting the FOV in this manner does not allow mapping over an extended area, it does decrease significantly both the engineering time and the overall cost of the proposed instruments. Both of these systems will support the data rate required for mapping but will lack the optical scanner that is needed for probing in two dimensions. Such a scanner could easily be added to the system in the future (i.e., under support by an industrial partner or in a future funding year).

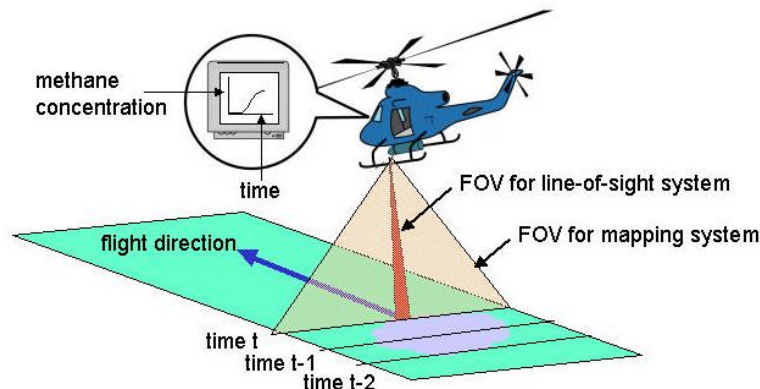


Fig. 19. Illustration of airborne instrument deployment (modified from Fig. 2).

Active System

Examination of active detection performance showed that the instrument factors limiting system performance vary with the standoff distance to the target. At short distances, laser speckle and laser energy fluctuations limit the system performance; average laser energy and detector performance limit the performance at longer distances. Thus, developing a long-standoff-distance instrument will require increasing the average laser energy and/or decreasing the detector noise. In addition, we have also experimentally confirmed that the minimum detectable limit improves as the square root of the number of averaged samples. Therefore averaging multiple data points acquired in the same FOV will improve the minimum detectable limit.

The available laser system used in the experiments over the past year produces $\sim 10 \mu\text{J}$ pulses of $3.3\text{-}\mu\text{m}$ light at 120 Hz. There are several options available that could produce greater pulse energy and/or greater repetition rates in a similarly portable package. To compare these specifications with the current laser system, we can expect approximately 10% conversion efficiency from the Nd:YAG laser wavelength to the $3.3 \mu\text{m}$ light that is absorbed by methane. Therefore, we can expect similar pulse energies at $3.3 \mu\text{m}$ when compared to the current laser system, but at significantly increased repetition rates. Because these lasers will likely not possess the narrow spectral linewidth of the current laser system, we will no longer be able to probe the R-branch transition, but instead will probe the broad Q-branch of methane at 3018 cm^{-1} . However, our modeling of the system performance enables prediction of the implications of this design. The spectra pictured in Fig. 20(a) and (b), respectively, show the R-branch and Q-branch of 10 ppm-m methane present in 0.038 atm-m water vapor.

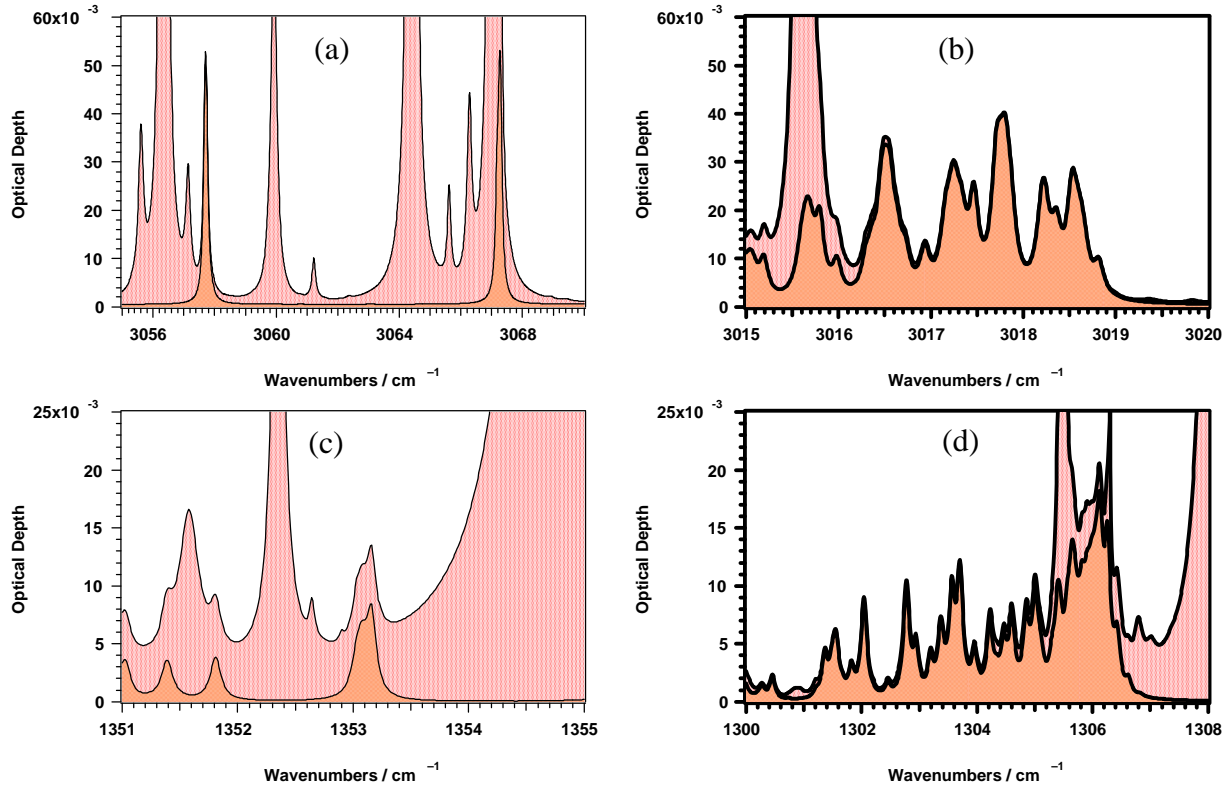


Fig. 20. Spectra of 10 ppm-m methane in 0.038 atm-m water vapor: (a) R-branch in mid-IR, (b) Q-branch in mid-IR, (c) R-branch in far-IR, (d) Q-branch in far-IR. The features in the forefront represent the absorption of methane while the features in the background represent the total absorption (methane plus water vapor).

In addition to replacing the current laser system, the detector characteristics could also be improved. At long ranges the current system is limited by both preamplifier noise and the background thermal radiation propagating towards the detector. These limitations will both be overcome by cooling the preamplifier and interference filter. Fig. 21(a) contains the components for the active detection system. Fig. 22 displays the predicted performance of the active system with the proposed laser system producing 10- μJ pulses at 10 kHz.

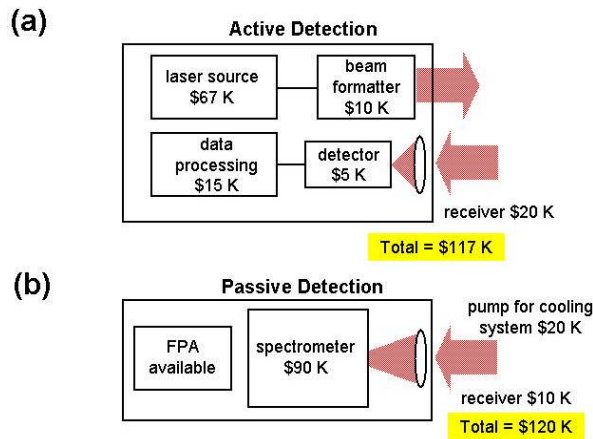


Fig. 21. Components of proposed (a) active and (b) passive detection systems

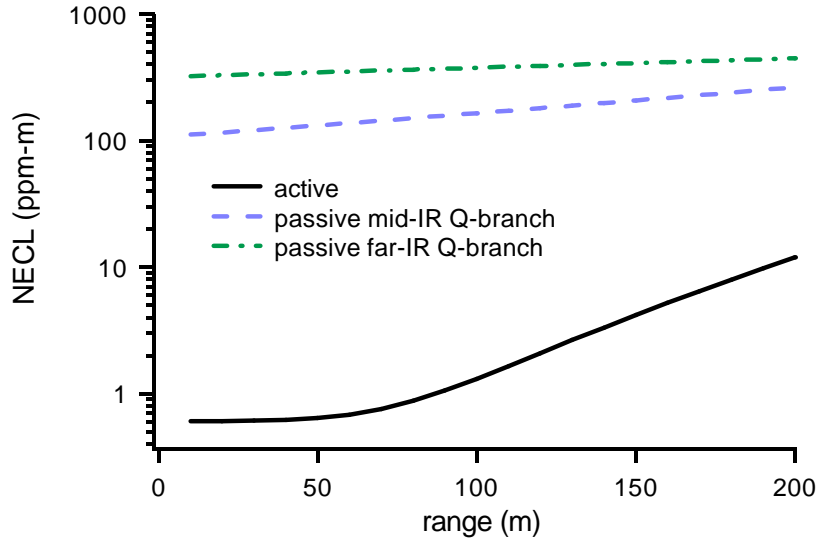


Fig. 22. NECLs for active and passive detection along a single line-of-sight. A 5°C temperature difference is assumed in the calculations, and the signal attenuation due to ambient methane is included.

Passive System

The critical specifications of a passive system are the spectral width of the filtering scheme and the detector noise. The spectral width must be narrow enough to match roughly the absorption feature of the gas, because radiation outside the absorption feature acts as a background noise. However, the instrument loses photons if the spectral width is too narrow, even if it is well-matched to a narrow absorption feature, resulting in the instrument being photon limited. For passive detection of methane plumes, we have considered probing the mid-IR Q-branch [Fig. 20(b)], and the far-IR Q-branch [Fig. 20(d)]. The far-IR R-branch [Fig. 20(c)] is not feasible for detection due to its overlap with water vapor absorption. Fig. 22 shows the relative NECL for probing different absorption features with optimally matched filtering systems. It assumes the characteristics of an IR focal plane array that is available in our laboratory for implementation into a breadboard system, with $\sim 300\text{ e}^{-}$ read noise and a 9.3-msec integration time. The integration time is defined by the required repetition rate of 107 Hz, determined from a flight speed of 120 mph and a desired 0.5-m resolution. Otherwise, the system parameters are identical to those listed in Table 7, with the exception that the imaging optics have been improved to $f\# / 1$ for better comparison to the active system.

From the two options displayed in Fig. 22, probing the mid-IR Q-branch at 3018 cm^{-1} appears the optimum solution for passive detection from a low-flying aircraft. While the thermal radiation produces 100 times more photons at 1303 cm^{-1} (as compared to 3018 cm^{-1}), the passive detection method is limited by the contrast between the gas and the surroundings, rather than the total number of photons collected. The lower absorptivity of the Q-branch at 1303 cm^{-1} results in a detection limit three times worse for the Q-branch in the long-IR. Therefore, to achieve the optimum sensitivity for reliable detection of methane, we would tune the passive detection system to the Q-branch of methane centered at 3018 cm^{-1} , which has a width of $\sim 3\text{ cm}^{-1}$. A cooled infrared spectrometer would provide the narrow bandwidth required for the optimum detection limit matched to the absorption feature. The passive-system components are displayed in Fig. 21(b). The NECLs for passive detection in Fig. 22 are plotted up to a detection range of 200 m. Assuming the minimum detectable limit is at least 3 times the NECL, above this altitude

would result in a minimum detectable limit of 400 ppm-m, which is larger than the majority of leak scenarios considered in Section 4. We acknowledge that as the performance characteristics of IR FPAs improve, the detection limit of passive sensing will also improve. However, even with a noiseless FPA the passive detection limit will be fundamentally limited by the amount of radiation collected from the scene. Setting all other noise sources to zero, background-limited detection can yield an NECL only as low as ~30 ppm-m for the methane mid-IR Q-branch; for the far-IR Q-branch, the background-limited NECL improves to 7 ppm-m because of the larger photon flux.

Detection Scheme Final Decision and Implementation

Based on the results of this study, we have decided to construct and test an active detection system for future implementation on a low-flying aircraft. The significantly superior predicted (and demonstrated) performance of active detection of methane justifies the decision. For a 200-m standoff distance, active detection demonstrates ~10 times more sensitivity than passive detection using available technology. However, we emphasize that this comparison between active and passive sensing applies only to the detection of methane; spectrally broader absorbers may be favorably detected with a passive approach.

The system design is currently in development, but with the experience of constructing shorter-range standoff gas detectors, we can estimate the characteristics for an airborne system. These system parameters are listed in Table 8. While potential designs of the laser source and beam formatter are being evaluated, these details are currently of a proprietary nature and cannot yet be released.

Table 8. Approximate specifications for airborne system.

Specification	Value
Size	0.5 m ³
Weight	40 kg
Power consumption	500 W

For initial airborne test of the instrument, Ross Aviation in Albuquerque operates a number of aircraft for both freight and passenger use for the DOE. Among the DOE aircraft are two DeHaviland Twin Otters, a two engine, 20-passenger, short-takeoff-and-landing aircraft (see Fig. 23). The Twin Otter has been used extensively for a variety of Sandia and other national lab research including atmospheric sampling, synthetic aperture radar development, a projectile dropping platform, airborne control platform for UAV development, airborne photography, as well as many other applications. FAA approvals have been obtained for flying the aircraft with the cargo doors removed. In this configuration, remote sensing instrumentation packages can be easily positioned inside the aircraft and oriented oriented to look obliquely at the ground through the side door opening. The Twin Otter also has a bottom viewing port such that an instrumentation system could also be palletized and configured for a downward looking orientation. The Twin Otter is available for a \$1000/day base-use fee with additional charges of \$500/hour incurred for flight time. The approximate costs for installation of a palletized instrument and 20 hours of flight time, assuming an experiment duration of three weeks, would be ~\$25K. Through our NETL-funded projects, we have established working relationships with pipeline companies who do routine maintenance and as a result may be venting lines (e.g., Duke Energy and Public Service Company of New Mexico). We could use these pipeline maintenance

operations as a target of opportunity and arrange with the maintenance crews to control the gas venting at a known rate while we are looking at the leak with an instrument installed in the Twin Otter.



Fig. 23. Twin Otter research aircraft

9. References

1. T. A. Reichardt, R. P. Bambha, T. J. Kulp, and R. L. Schmitt, "A frequency-locked, injection-seeded, pulsed narrowband optical parametric generator," submitted to *Appl. Opt.* (2002).
2. T. G. McRae, "Evaluation of a new aerial leak survey approach," Report GRI-96/0376, Gas Research Institute, Chicago, IL (1996).
3. D. Flanigan, "Detection of organic vapors with active and passive sensors: a comparison," *Appl. Opt.* **25**, 4253-4260 (1986).
4. T. A. Reichardt, S. Devdas, W. Einfeld, and T. J. Kulp, "Evaluation of active and passive gas imagers for transmission pipeline remote leak detection: Summary design report of breadboard systems," submitted to NETL (2002).
5. A. Minato, M. A. Joarder, S. Ozawa, M. Kadoya, and N. Sugimoto, "Development of a lidar system for measuring methane using a gas correlation method," *Jpn. J. of Appl. Phys.* **38**, 6130-6132 (1999).
6. J. Sandsten, P. Weibring, H. Edner, and S. Svanberg, "Real-time gas-correlation imaging employing thermal background radiation," *Opt. Express* **6**, 92-103 (2000).
7. T. Iseki, H. Tai, and K. Kimura, "A portable remote methane sensor using a tunable diode laser," *Meas. Sci. Technol.* **11**, 594-602 (2000).

8. I. Dubinsky, K. Rybak, J. I. Steinfeld, and R. W. Field, "Frequency-modulation-enhanced remote sensing," *Appl. Phys. B* **67**, 481-492 (1998).
9. R. T. Wainner, B. D. Green, M. G. Allen, M. A. White, J. Stafford-Evans, and R. Naper, "Handheld, battery-powered near-IR TDL sensor for stand-off detection of gas and vapor plumes," *Appl. Phys B* **75**, 249-254 (2002).